Reverse Total Shoulder Arthroplasty Baseplate Stability in Superior Bone Loss With Augmented Implant

Elise J Martin, PhD[1,2] ⓘD, Thomas R Duquin, MD[2], and
Mark T Ehrensberger, PhD[1,2]

Abstract

Background: Glenoid bone loss is commonly encountered in cases of rotator cuff tear arthropathy and can create challenges during reverse shoulder arthroplasty. In this study, we sought to investigate the biomechanical properties of a new treatment option for superior glenoid defect, an augmented reverse total shoulder baseplate.

Methods: Three conditions were examined: non-augmented baseplate without defect, non-augmented baseplate with defect, and augmented baseplate with defect. The augmented baseplates included a 30-degree half wedge which also matched the created superior defect. The samples were cyclically loaded at a $60°$ simulated abduction angle to mimic baseplate loosening. The migration and micromotion of the baseplate were measured on the superior edge using a 3D Digital Image Correlation System.

Results: The migration measured in the augmented baseplate showed no significant difference when compared to the no defect or defect cases. In terms of micromotion, the augmented baseplate showed values that were between the micro-motions reported for the no defect and defect conditions, but not by a statistically significant amount.

Conclusion: This study provides biomechanical evidence that augmented baseplates can reduce the amount of micro-motion experienced by the RSA construct in the presence of significant superior glenoid bone deficiency, but do not fully restore stability to that of a full contact non-augmented baseplate.

Keywords

Reverse shoulder arthroplasty, glenoid baseplate, augment, biomechanics, superior defect, 3D DIC

Introduction

Reverse total shoulder arthroplasty (RSA) is a successful treatment option for patients with rotator cuff tear arthropathy. However, concern remains regarding the long-term results of RSA and potential for implant loosening, especially in the presence of glenoid bone defects.[1,2] Unfortunately, glenoid bone deficiency is common in patients undergoing RSA. As many as 63% of patients undergoing reverse total shoulder arthroplasty have some form of glenoid wear prior to surgery, with 9% of patients presenting with significant superior glenoid bone deficiency.[2] Primary methods of managing bone deficiency in RSA include bone grafting and eccentric reaming. These techniques show mixed long-term results, with concerns regarding implant stability, joint line medialization, and bone graft resorption.[2–6]

Augmented baseplates are now available for the management of glenoid bone deficiency in RSA. There are several different augmented RSA designs currently approved for clinical use; these implants include an additional metal augment that accommodates glenoid bone deficiency without the need for excessive eccentric reaming or bone grafting. Some augmented baseplates are

[1]Department of Biomedical Engineering, State University of New York at Buffalo, Buffalo, New York
[2]Department of Orthopaedic Surgery, State University of New York at Buffalo, Buffalo, New York

Corresponding Author:
Mark T Ehrensberger, Department of Biomedical Engineering, State University of New York at Buffalo, 3435 Main Street, 445 Biomedical Research Building, Buffalo, NY 14214, USA.
Email: mte@buffalo.edu

designed to work in conjunction with eccentric reaming in an attempt to reduce bone removal prior to implantation. Augmented baseplates are an innovative solution to glenoid bone loss with good clinical outcomes. However, the available literature is limited, and only reports the short to mid-term outcome of augmented implants.[7–10] Laboratory mechanical testing of glenoid bone deficiency in reverse total shoulder arthroplasty demonstrates compromised implant stability in the presence of significant glenoid bone deficiency with traditional implants.[11–14] Other studies have examined the biomechanics of specific augmented baseplate designs, typically designed to compensate for small glenoid defects.[13,15] These two studies examined the use of a full wedge augmented baseplate in conjunction with off-axis reaming compared to a standard baseplate in conjunction with eccentric reaming, and determined that both setups were viable options for RSA.[13,15] The goal of this biomechanical laboratory study is to evaluate the initial fixation stability of an half-wedge augmented baseplate in the presence of a large superior glenoid bone deficiency compared to a non-augmented baseplate in the presence or absence of a large superior glenoid bone deficiency. Our hypothesis is that an augmented baseplate will demonstrate improved stability in the presence of bone deficiency compared to a non-augmented baseplate, and will be similar to a non-augmented baseplate with full backing support.

Materials and Methods

Specimen Preparation

Thirty samples of solid rigid polyurethane bone foam (Sawbone Inc., Vashon, WA, USA) were machined into cylinders with a diameter of 40 mm and a height of 80 mm; the last 15 mm at the height of the sawbone was tapered inward to create a smaller diameter of 30 mm at the end face of the material to model the glenoid. The bone foam material used had a density of 0.320 g/cm^3 (20 pounds/cubic foot [pcf]), a compressive strength of 8.40 MPa, and a compressive modulus of 210 MPa.[16] A 30 degree wedge was subsequently removed from the glenoid face from twenty bone foam samples to produce a simulated superior glenoid bone defect that resulted in only 50% of the baseplate having underlying bone foam support. The remaining ten samples were left intact to act as a no defect control condition. All bone foam samples were embedded within polymethylmethacrylate (PMMA) cement so that 1 cm of bone foam was exposed.

The Comprehensive Reverse Total Shoulder Prosthesis system (Zimmer Biomet, Warsaw, IN) was utilized for this trial. The baseplates were implanted according to the manufacturer's recommended technique. Non-augmented baseplates (diameter 25 mm) were fixed to the prepared bone foam samples using a 30 mm central screw and four locking peripheral screws (15 mm anterior/posterior and 30 mm superior/inferior). The augmented baseplate used was also 25 mm in diameter with a 30 degree half wedge and was secured with the same screw configuration as the non-augmented baseplate. A 36 mm glenosphere with no lateral offset and 3.5 mm inferior offset was used for all tests. Three specific baseplate-substrate configurations were assessed in this study: non-augmented baseplate without bone defect ("no defect" condition), non-augmented baseplate with bone defect ("defect" condition), and the augmented baseplate with bone defect ("augment" condition).

Following implantation, the constructs were spray painted to achieve a speckled stochastic pattern on the exposed surfaces of the baseplate and bone foam to be used for a full-field displacement analysis using 3D digital image correlation. The final prepared test constructs are shown in Figure 1.

The test constructs were then secured within an aluminum cylinder that was rigidly mounted to the base of a servo-hydraulic load frame (mini-Bionix II, MTS Corp., Eden Prairie, MN) such that the superior-inferior axis of the glenoid was oriented at 60° relative to the vertical axis of the load frame actuator (Figure 2(A)). This orientation produces a maximum joint reaction force via a simulated 60 degrees of abduction.[17] As described in previous work, this angle will produce a 0–650 N normal force and a 0–375N superior shear force.[12] The glenosphere was then impacted onto the baseplate and the humeral tray and poly liner were mounted to the actuator of the load frame. Mechanical testing was performed by cyclically compressing the humeral tray onto the glenosphere from 0 N to 750 N at 1 Hz for a total of 5000 cycles.

Data Analysis

A 3D Digital Image Correlation (DIC) system (ARAMIS Stereo Camera System; GOM GmbH, Braunschweig, Germany) was utilized to perform a full-field displacement analysis of the test construct during the mechanical testing. The ARAMIS 3D DIC camera system (two 2.3 M pixel cameras with Schneider 50 mm lenses and 10 mm distance ring) was positioned at a working distance of 175 mm from the superior edge of the sample (Figure 2(B)) to gain a full view of the superior edge of the implant as well as the supporting sawbone as shown in camera snapshots in Figure 3. The camera setup has a 1936 × 1261 pixel camera resolution, and with the selected field of view used in this study (75/45/25 mm) a measurement sensitivity of 0.37 microns in plane and 1.11 microns out of plane was achieved.
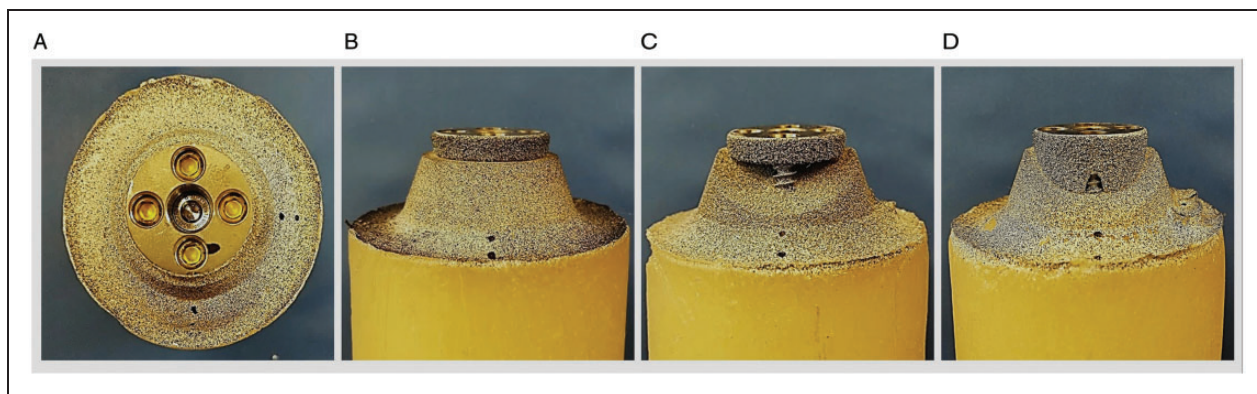
Figure 1. Selected samples shown implanted, potted, and spray painted in preparation for testing. A, Top down view of a non-augmented baseplate. The most superior (bottom) and most anterior (right) points are marked with permanent marker so they are more easily identified in the camera images. B, Superior view of a non-augmented baseplate implanted with no defect. C, Superior view of a non-augmented baseplate implanted with 50% defect. D, Superior view of an augmented baseplate implanted with 50% defect.
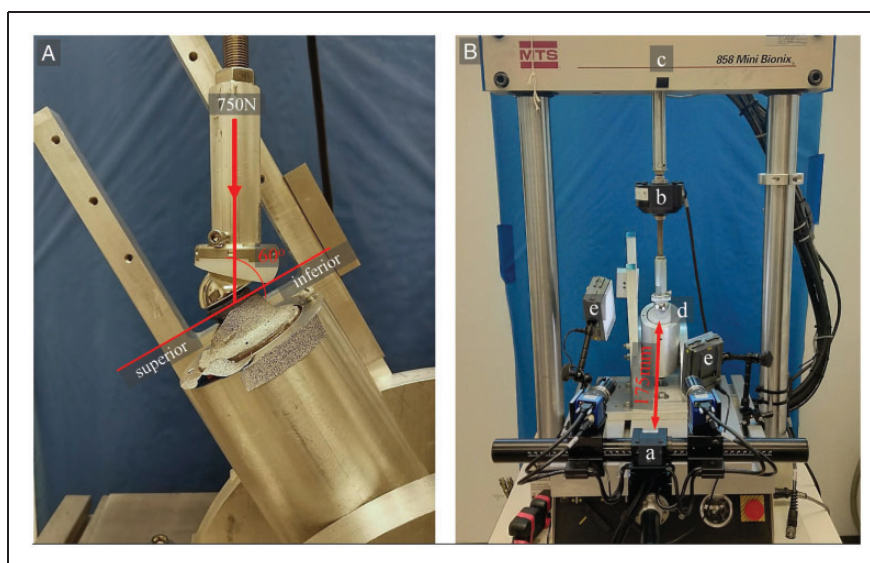

Figure 2. Setup of sample within load frame. A, Anterior view, illustration of 60o application of 750N force. B, Superior view of setup within load frame, illustrating 175 mm working distance for camera system: (a) ARAMIS camera system, (b) load cell, (c) hydraulic load frame, (d) mounted sample, (e) light source.
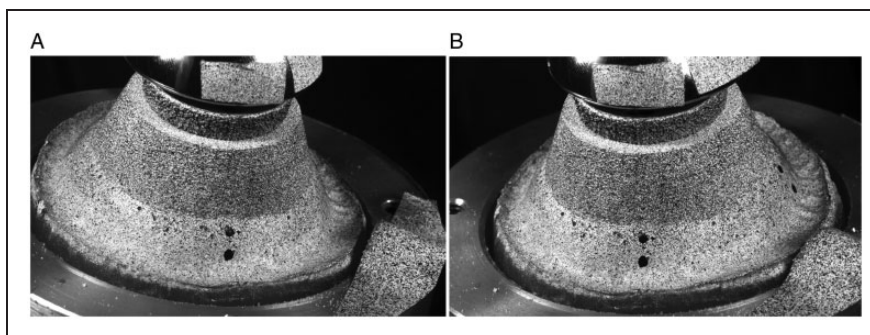

Figure 3. Full field of view of a selected sample taken by ARAMIS 3D DIC Camera System. A, Image from left camera. B, Image from right camera.

The digital image correlation method has been used in many different areas of biomechanics including bone and tissue strain analysis,[18,19] dental applications,[20,21] and knee and hip arthroplasty,[22–26] as it allows for full field measurements of displacement and strain. The camera system collected full-field displacement data at 10 frames per second at specified intervals during the testing. This data was collected during the initial 10 cycles of loading, followed by 10 cycle data sets collected every 100 cycles for the first 1,000 cycles and then every 500 cycles up to 5,000 cycles. In addition, the output of load cell from the load frame was captured during the test and synced to the displacement data collected with the camera system.

The displacement data captured with the camera system was further analyzed within the GOM Correlate Professional software (GOM GmbH, Braunschweig, Germany). The same coordinate frame was applied to all images with the origin of the reference axes defined at the most superior point on the baseplate edge, and the axes oriented so that positive Y was superior, positive X was anterior, and positive Z was medial (Figure 4(A)). Motion analysis was focused on displacement in the inferior/superior direction, medial/lateral direction and total motion (vector sum of Y and Z displacement). There were two principle analysis techniques utilized. In the first technique, the CAD models for the baseplates were imported into the software and aligned by a best-fit algorithm to the baseplate surfaces that were visible in

the camera images. Subsequently, utilizing rigid body mechanics, the motion of the region of the baseplate visible to the camera could be utilized to define the motion at any point on the CAD model, including points not directly visible to the camera. The specific points of interest in this study were the most superior point, the most inferior point, and the tip point at the end of the glenoid baseplate central stem (Figure 4(B)). The motion of the superior, inferior, and tip points were then normalized relative to the position of the aluminum support cylinder that rigidly held the test constructs. This normalized motion was defined as baseplate global motion, and includes strain within the sawbone as well as any displacement between the baseplate and sawbone. The second analysis technique utilized the software to create a virtual displacement gauge with endpoints defined at the most superior point on the baseplate and the sawbone directly medial to it along the Z axis. These displacement gauges provide direct measurement of relative motion between the superior edge of the baseplate and the sawbone and are defined as baseplate interfacial motion (Figure 4(C) and (D)). This interfacial motion analysis was reported only for the defect and augment conditions because both of these conditions had identical sawbone substrates (wedge defect) and therefore identical gauge lengths and endpoint locations could be utilized for meaningful comparison.

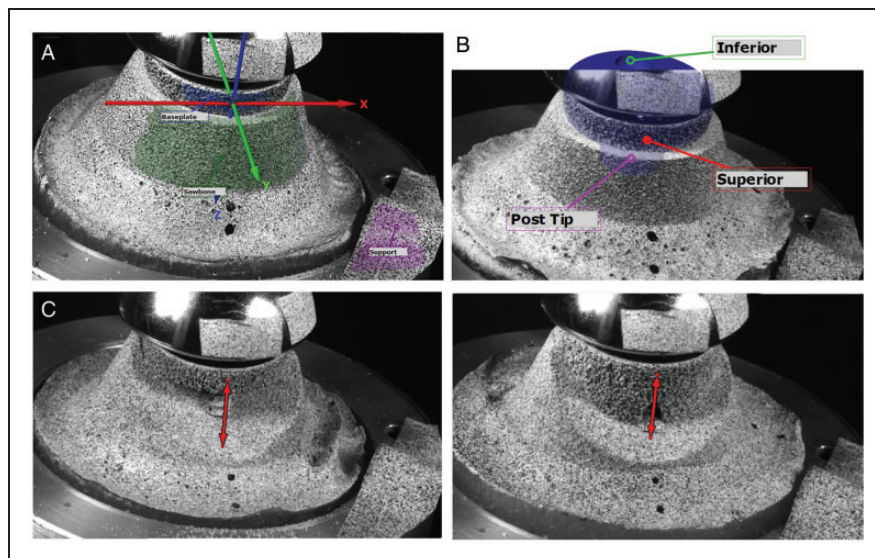The global and interfacial motion data and the load data were further analyzed with a custom LabView

Figure 4. Modifications are made to the camera images to allow for further analysis. A, The axis is defined as well as the surfaces of interest: baseplate, sawbone, and support. B, Measurement of global motion. The CAD file for this implant is imported into the data and aligned with the surfaces visible to the camera. This allows for analysis of points not directly visible by the camera. Modifications are made to the camera images to allow for further analysis. A, The axis is defined as well as the surfaces of interest: baseplate, sawbone, and support. B, Measurement of global motion. The CAD file for this implant is imported into the data and aligned with the surfaces visible to the camera. This allows for analysis of points not directly visible by the camera. C/D, Measurement of interfacial motion. Virtual superior strain gauge for both the defect (C) and augment cases.

program (LabView 2016; National Instruments Corp., Austin, TX, USA), to identify the baseplate point displacements where the load frame was applying maximum force (750N) and minimum force (0N). These displacements at maximum load and minimum load were averaged across each set of 10 cycles collected. Finally, the averaged displacements at maximum and minimum load were used to calculate migration and micromotion values. Migration was calculated by subtracting the averaged displacement at minimum load, as determined from each test collection interval, from the initial unloaded position at the beginning of the test. Micromotion was calculated for each test collection interval by subtracting the averaged displacement at minimum load from the averaged displacement at maximum load.

Statistical Analysis

The displacements measured for migration and micromotion were compared between no defect, defect, and augment for each point of interest. This comparison was completed for all cycle counts but our primary focus was on the initial and final cycles. In most cases, an analysis of variance (ANOVA) followed by a Tukey post hoc was performed. In cases where a Levene's test was

significant, the comparison was completed with a Welch test followed by a Games-Howell post hoc. Statistical analysis was performed using SPSS 25 (IBM, Armonk, NY, USA). In all tests, a $P \leq 0.05$ was considered significant.

Results

Global Motion

The global migration and global micromotion of the selected points on the CAD import are presented in Table 1 and Table 2 respectively, for the initial (cycles 0–10) and final (cycles 4990–5000) data collections. The data is further categorized into medial displacement and superior displacement of the superior edge, inferior edge, and post tip.

The amount of migration was not significantly different between sample groups in either the initial or final cycle counts. The trends for the total migration (Figure 5 (A) and (C)) illustrate an increase in the migration throughout the test on both the superior and inferior edges indicating that all sample types migrate to some extent during the test. As seen in previous tests,[12] the migration has an asymptotic increase throughout the

Table 1. Global Migration Values (Mean $\pm$ Standard Deviation).

	Initial migration (um)			P Value		
Variable	No Defect	Augment	Defect	No Defect vs. Augment	No Defect vs. Defect	Defect vs. Augment
Superior edge						
Medial displacement	0.23 ± 4.64	0.04 ± 4.50	6.55 ± 15.44	1.00	0.34	0.31
Superior Displacement	1.63 ± 2.73	0.19 ± 3.20	0.52 ± 5.09	0.93	0.97	1.00
Inferior Edge						
Medial Displacement	-7.42 ± 8.99	0.66 ± 5.82	5.26 ± 16.86	0.38	0.05	0.84
Superior Displacement	1.44 ± 3.03	0.14 ± 3.05	0.40 ± 5.12	0.95	0.98	1.00
Post Tip Edge						
Medial Displacement	-3.68 ± 4.56	0.23 ± 4.44	6.10 ± 15.60	0.81	0.27	0.49
Superior Displacement	-2.15 ± 6.31	0.44 ± 2.16	0.06 ± 5.98	0.70	0.81	1.00

	Final migration (um)			P Value		
Variable	No Defect	Augment	Defect	No Defect vs. Augment	No Defect vs. Defect	Defect vs. Augment
Superior edge						
Medial displacement	39.40 ± 59.82	23.83 ± 20.20	25.30 ± 42.03	0.86	0.90	1.00
Superior Displacement	33.44 ± 26.15	46.66 ± 33.10	64.43 ± 55.64	0.91	0.27	0.77
Inferior Edge						
Medial Displacement	5.52 ± 59.71	-2.12 ± 33.91	-17.61 ± 34.42	0.99	0.70	0.91
Superior Displacement	31.96 ± 24.76	$44 .69 \pm 32.26$	62.15 ± 52.89	0.91	0.26	0.76
Post Tip Edge						
Medial Displacement	23.18 ± 57.69	11.76 ± 25.25	4.82 ± 27.99	0.95	0.77	0.99
Superior Displacement	17.22 ± 17.02	33.51 ± 23.94	42.70 ± 39.33	0.62	0.19	0.93

Table 2. Global Micromotion Values (Mean ± Standard Deviation).

Variable	Initial Micromotion (um)			P Value		
	No Defect	Augment	Defect	No Defect vs. Augment	No Defect vs. Defect	Defect vs. Augment
Superior edge						
Medial displacement	61.42 ± 25.52	85.50 ± 24.04	109.30 ± 29.60	0.28	0.02	0.29
Superior Displacement	79.31 ± 21.56	97.16 ± 28.10	121.49 ± 23.46	0.31	0.00	0.08
Inferior Edge						
Medial displacement	36.07 ± 24.81	35.23 ± 25.67	41.44 ± 43.86	1.00	0.98	0.97
Superior Displacement	78.44 ± 19.57	94.19 ± 25.44	116.02 ± 18.28	0.35	0.01	0.09
Post Tip Edge						
Medial Displacement	49.85 ± 24.39	62.82 ± 24.23	78.88 ± 43.75	0.75	0.07	0.58
Superior Displacement	66.53 ± 18.26	75.04 ± 20.42	86.29 ± 18.63	0.83	0.13	0.65
	Final Micromotion (um)			P Value		
	No Defect	Augment	Defect	No Defect vs. Augment	No Defect vs. Defect	Defect vs. Augment
Superior edge						
Medial displacement	59.58 ± 27.87	79.95 ± 15.87	102.91 ± 28.63	0.41	0.05	0.29
Superior Displacement	75.12 ± 20.26	90.81 ± 24.29	112.37 ± 22.76	0.36	0.01	0.10
Inferior Edge						
Medial displacement	35.04 ± 27.54	33.07 ± 18.33	42.19 ± 42.81	1.00	0.95	0.89
Superior Displacement	74.23 ± 18.98	87.26 ± 21.95	107.54 ± 20.15	0.49	0.01	0.10
Post Tip Edge						
Medial Displacement	48.35 ± 26.98	58.94 ± 16.07	75.80 ± 43.52	0.85	0.09	0.51
Superior Displacement	63.14 ± 18.62	70.17 ± 17.37	80.94 ± 16.67	0.91	0.23	0.70

course of testing, showing most migration within the first 1000 cycles.

As reported in Table 2, significantly greater initial micromotion was reported for the defect condition versus the no defect condition when evaluating the medial (defect $109.3 ± 29.6\,\mu m$ vs no defect $61.4 ± 25.5\,\mu m$, $p < 0.01$) and superior (defect $121.5 ± 23.5\,\mu m$ vs no defect $79.3 ± 21.6\,\mu m$, $p < 0.01$) micromotions of the superior edge, and the superior micromotion (defect $116.0 ± 18.3\,\mu m$ vs no defect $78.4 ± 19.6\,\mu m$, $p < 0.01$) of the inferior edge. These same relationships were also reported at the end of the test where the defect condition had significantly greater final micromotion compared to the no defect condition in terms of the medial (defect $102.9 ± 28.6\,\mu m$ vs no defect $59.6 ± 27.9\,\mu m$, $p < 0.01$) and superior (defect $112.4 ± 22.8\,\mu m$ vs no defect $75.1 ± 20.3\,\mu m$, $p < 0.01$) micromotions of the superior edge, and the superior micromotion (defect $107.6 ± 20.2\,\mu m$ vs no defect $74.2 ± 19.0\,\mu m$, $p < 0.01$) of the inferior edge. The augment condition showed initial and final micromotion values that were between the micromotions reported at all locations for the no defect and defect conditions. There were no significant differences when the initial or final micromotions of the augment condition were compared to either the no defect or defect condition (Table 2). The total micromotion across cycle counts (Figure 5(B) and (D)) shows a similar trend for all test conditions and a consistent amount of micromotion through the entire test sequence. Additionally, it is shown that the amount of motion experience by the augment condition is in between the amount of micromotion experienced in the no defect and defect conditions both on the inferior and superior edges.

Interfacial Motion

The interfacial migration and interfacial micromotion of the virtual displacement gauge on the superior edge of the test constructs are shown in Table 3 and Table 4 respectively, for the initial (cycles 0–10) and final (cycles 4990–5000) data collections. The data is further categorized into medial displacement, superior displacement, and total displacement. As with the global motion values, there is no significant difference between the defect and augment condition when examining the initial and final migration values. In terms of micromotion on the superior edge, the augment condition showed significantly less micromotion in all cases compared to the defect condition both initially and during the final cycles.
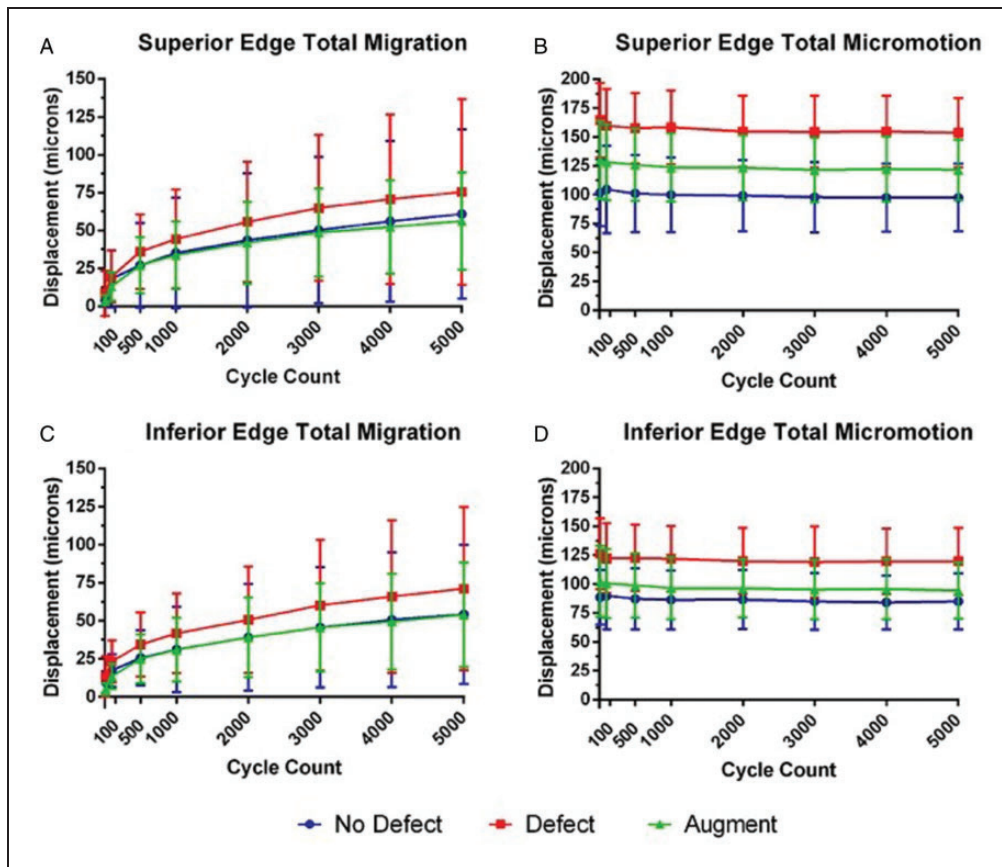
Figure 5. Plots of the global migration of the (A) superior edge and (C) inferior edge and global micromotion of the (B) superior edge and (D) inferior edge for selected cycle counts throughout testing. The values represent average total motion and are presented as the mean value ± 1 standard deviation.

Table 3. Intel'facial Interfacial Migration Values (Mean $\pm$ Standard Deviation).

	Initial migration (um)		
Variable	Augment	Defect	P value
Medial Displacement	0.21 ± 0.47	-0.11 ± 0.65	0.97
Superior Displacement	0.88 ± 1.46	0.23 ± 0.90	0.91
Total Displacement	1.32 ± 1.16	1.30 ± 0.86	1.00

	Final migration (um)		
Variable	Augment	Defect	P value
Medial Displacement	2.72 ± 1.80	3.77 ± 1.73	0.83
Superior Displacement	14.78 ± 9.09	15.79 ± 3.78	0.99
Total Displacement	15.43 ± 8.49	16.30 ± 3.20	0.99

Table 4. Interfacial Micromotion Values (Mean $\pm$ Standard Deviation).

	Initial migration (um)		
Variable	Augment	Defect	P value
Medial displacement	28.37 ± 12.86	46.69 ± 8.02	0.03
Superior displacement	46.64 ± 14.77	70.00 ± 9.58	0.01
Total displacement	56.72 ± 10.69	83.40 ± 10.26	0.02

	Final migration (um)		
Variable	Augment	Defect	P value
Medial displacement	27.99 ± 11.23	46.02 ± 7.48	0.02
Superior displacement	45.94 ± 14.29	68.00 ± 8.69	0.09
Total displacement	55.03 ± 10.13	81.56 ± 9.85	0.01

Discussion

The purpose of this study was to assess the stability of an augmented baseplate compared to a non-augmented baseplate in the presence or absence of a superior glenoid bone defect utilizing a previously published biomechanical testing protocol.[12] The results of the global motion analysis indicated that the presence of a 50% bone defect of the superior glenoid significantly increases the global micromotion on the superior edge of the non-augmented baseplate. This finding is consistent with previous reports showing that glenoid bone defects reduce baseplate stability.[11–13] Furthermore, the

global motion analysis showed that the average global micromotion values of the augmented baseplate were smaller than the values reported for the non-augmented baseplate in the presence of the bone defect, and larger than the values reported for the non-augmented baseplate without the bone defect. Interestingly, these differences were not statistically significant. However, further analysis utilizing virtual displacement gauges to precisely quantify the baseplate-substrate interfacial motion showed that the augmented baseplate had statistically significantly smaller interfacial micromotion on the superior edge as compared to the non-augmented baseplate with the bone defect. This study provides biomechanical evidence that augmented baseplates can reduce the amount of micromotion experienced by the RSA construct in the presence of significant superior glenoid bone deficiency.

The migration values (both global and interfacial measurements) increased during testing for each test construct. As seen in previous tests,[12] the total migration reported here has an asymptotic increase throughout the course of testing, showing most migration within the first 1000 cycles. There were no significant differences in migration when comparing across all test condition groups. This indicates that some degree of migration is inherent as each construct settles into the substrate during testing.

There are several choices made when designing this study to test in the most accurate way possible, while also optimizing data collection and the analysis process. As described in a previously published study,[12] we utilized a simulated abduction model. Although there are several different models utilized for RSA baseplate testing, we chose this model because it closely mimics the forces at the most extreme inferior potion of the ASTMs cyclic rotation model while also permitting for continuous measurement of baseplate displacement. Additionally, the ASTM for testing of RSA glenoid baseplate loosening recommends utilizing bone substrate that is of 15–20pcf.[27] We chose to use 20pcf because it is within the parameters for glenoid bone stock in the typical RSA recipient,[28] and also provides more testing consistency between samples when compared to cadaveric samples which typically have significant anatomic variation. Since the primary goal of this experiment was to compare between different constructs, we want to reduce inconsistencies due to very low-density bone substitute. Finally, because we are using a model with no biological influence, and therefore examining initial fixation of the baseplate, we only tested to 5,000 cycles which sufficiently models any forces experienced prior to assistance from biological impact. Additionally, previous work has indicated that the amount of displacement does not significantly change after 1,000 cycles in similar biomechanical studies.[12] This study utilized a 3D DIC system to characterize the motion of glenoid baseplates. The 3D DIC method has been used in many different areas of biomechanics including bone and tissue strain analysis,[18,19] dental applications,[20,21] and knee and hip arthroplasty,[22–26] as it allows for full field measurements of displacement and strain. The use of the high definition ARAMIS 3D DIC system provides many advantages to assess the stability of the baseplate. This system can track the 3-dimensional displacement of multiple regions of interest with high spatial resolution without having to directly contact the test sample. This non-contact approach ensures that the measurement device/sensor is not physically influencing the motion of the baseplate. In addition, the system allowed for several post-processing analysis techniques to be performed on the images captured during the test. For example, CAD models of the baseplates were imported, aligned, and synchronized to the motion captured by the cameras during testing and subsequent rigid body mechanics calculations were able to assess motion of regions of the implant not directly visible to the cameras in the original motion capture. In addition, virtual displacement gauges can be applied to the motion capture images via post-processing techniques and be used to track relative motion between different regions of interest throughout the testing sequence. A combination of these techniques was utilized in the present study to report both the global and interfacial motion of the baseplate constructs.

The global motion analysis utilized the CAD import and rigid body mechanics to measure the amount of motion of specific baseplate locations relative to the support structure. This measurement of baseplate motion includes any displacement due to deformation of the bone foam substrate or embedding PMMA and any relative displacements at the construct interfaces (i.e. baseplate-bone foam, bone foam-PMMA, PMMA-support structure interfaces). It is possible that the global motion measurements contain displacement contributions from each of the above sources. The interfacial motion analysis utilized virtual displacement gauges to directly examine how the superior baseplate edge moves in relation to the bone foam directly below the baseplate edge. It is important to note the difference in magnitude between the global and interfacial values. For example, the superior edge micromotions reported for the augment and defect conditions are in the range of 80–120 microns for the global measurements and only 30–70 microns for the interfacial measurements. This difference indicates that values measured globally may be an overestimate of the motion that occurs directly between the bone foam and the baseplate.

Furthermore, it is important to point out that many previous studies have utilized externally mounted linear variable differential transformers (LVDTs) or dial gauges to track baseplate edge motions at specific

point locations on the baseplate during biomechanical testing. Typically, the motion measured with these devices is described as motion of the baseplate relative to the bone foam, and the underlying assumption is that there are no other sources of motion in the construct and that the bone foam substrate does not deform under loading. However, if this assumption were true, the interfacial motion measured in this study would have been equal to the global motion reported. The fact that the interfacial motion was smaller than the global motion indicates that there are likely other sources of motion within the test construct. Therefore, tests conducted where LVDTs or dial gauges are mounted on an external fixture and utilized to measure implant relative micromotion are also likely overestimates of the true interfacial motion between the baseplate and substrate. Based upon this analysis, it is suggested that future studies seeking to accurately measure the baseplate-substrate interfacial motion should consider use of a 3D DIC methodology rather than use of externally mounted LVDTs or dial gauges.

As with all biomechanical studies, there are few limitations with this testing method that make direct comparison to the clinical case difficult. Although our simulated abduction model does provide a simple model of shoulder force application, further work is needed to develop a more complex model that can rotate the implant through a more relevant abduction arc while maintaining our ability to collect measurements continuously. This type of test would provide invaluable information regarding the biomechanics of RSA. Additionally, we only tested one singular type and size of augmented baseplate. It would be interesting to examine the impact of different augment sizes in conjunction with different types of non-uniform glenoid defects that may more closely mimic anatomical defects both in size, shape, and location on the glenoid surface. Various iterations of studies of this type will vastly increase our understanding of the limitation of augmented baseplates, and how stability is affected by different anatomical conditions.

Conclusion

The use of an augmented baseplate in the presence of a large superior glenoid defect does enhance the stability of the construct when compared to a non-augmented baseplate implanted with the same large superior defect, but the augmented baseplate is not able to fully restore stability to that of the full contact non-augmented baseplate. These results indicate that this augmented baseplate could be a viable option for treatment of superior glenoid defects.

ORCID iD

Elise J Martin ⓘD https://orcid.org/0000-0002-6069-2868

References

1. Frankle MA, Teramoto A, Luo ZP, Levy JC, Pupello DR. Glenoid morphology in reverse shoulder arthroplasty: classification and surgical implications. *J Shoulder Elbow Surg*. 2009;18:874–885.
2. Gilot GJ. Addressing glenoid erosion in reverse total shoulder arthroplasty. *Bull Hosp Jt Dis*. 2013;71:S51–S53.
3. Neyton L, Boileau P, Nove-Josserand L, Edwards TB, Walch G. Glenoid bone grafting with a reverse design prosthesis. *J Shoulder Elbow Surg*. 2007;16:S71–S78.
4. Power I, Throckmorton TW. Reverse TSA with an augmented baseplate: dealing with glenoid deficiency. *Semin Arthroplast*. 2018;29:87–90.
5. Scalise JJ, Iannotti JP. Bone grafting severe glenoid defects in revision shoulder arthroplasty. *Clin Orthop Relat Res*. 2008;466:139–145.
6. Wagner E, Houdek MT, Griffith T, et al. Glenoid bone-grafting in revision to a reverse total shoulder arthroplasty. *J Bone Jt Surg*. 2015;97:1653–1660.
7. Virk M, Yip M, Liuzza L, et al. Clinical and radiographic outcomes with a posteriorly augmented glenoid for Walch B2, B3, and C glenoids in reverse total shoulder arthroplasty. *J Shoulder Elbow Surg*. 2020;29: e196–e204.
8. Liuzza L, Mai DH, Grey S, et al. Reverse total shoulder arthroplasty with a superior augmented glenoid component for favard type-E1, E2, and E3 glenoids. *J Bone Jt Surg*. 2020;102:1865–1873.
9. Wright TW, Roche CP, Wright L, Flurin PH, Crosby LA, Zuckerman JD. Reverse shoulder arthroplasty augments for glenoid wear: comparison of posterior augments to superior augments. *Bull Hosp Jt Dis*. 2015;73:S124.
10. Jones RB, Wright TW, Roche CP. Bone grafting the glenoid versus use of augmented glenoid baseplates with reverse shoulder arthroplasty. *Bull Hosp Jt Dis*. 2015;73: S129–S135.
11. Formaini NT, Everding NG, Levy JC, et al. The effect of glenoid bone loss on reverse shoulder arthroplasty baseplate fixation. *J Shoulder Elbow Surg*. 2015;24:e312– e319.
12. Martin EJ, Duquin TR, Ehrensberger MT. Reverse total shoulder glenoid baseplate stability with superior glenoid bone loss. *J Shoulder Elbow Surg*. 2017;26:1748–1755.

13. Roche C, Stroud NJ, Martin BL, et al. Achieving fixation in glenoids with superior wear using reverse shoulder arthroplasty. *J Shoulder Elbow Surg*. 2013;22:1695–1701.

14. Sutton LG, Werner FW, Jones AK, Close CA, Nanavati VN. Optimization of glenoid fixation in reverse shoulder arthroplasty using 3-dimensional modeling. *J Shoulder Elbow Surg*. 2010;19:664–669.

15. Friedman R, Stroud N, Glattke K, et al. The impact of posterior wear on reverse shoulder glenoid fixation. *Bull Hosp Jt Dis*. 2015;73:S15–S20.

16. Sawbones. Sawbones: biomechanical test materials. Accessed May 23, 2016. Published 2016. https://www.sawbones.com/media/assets/product/documents/biomechanical_catalog2020.pdf

17. Kwon YW, Forman RE, Walker PS, Zuckerman JD. Analysis of reverse total shoulder joint forces and glenoid fixation. *Bull Hosp Jt Dis*. 2010;68:273–280.

18. Väänänen SP, Amin Yavari S, Weinans H, Zadpoor AA, Jurvelin JS, Isaksson H. Repeatability of digital image correlation for measurement of surface strains in composite long bones. *J Biomech*. 2013;46:1928–1932.

19. Zhang DS, Arola DD. Applications of digital image correlation to biological tissues. *J Biomed Optics*. 2004;9:691–699.

20. Goellner M, Schmitt J, Karl M, Wichmann M, Holst S. Photogrammetric measurement of initial tooth displacement under tensile force. *Med Eng Phys*. 2010;32:883–888.

21. Tanasic I, Milic-Lemic A, Tihacek-Sojic L, Stancic I, Mitrovic N. Analysis of the compressive strain below the removable and fixed prosthesis in the posterior mandible using a digital image correlation method. *Biomec Model Mechanobiol*. 2012;11:751–758.

22. Small SR, Hensley SE, Cook PL, et al. Characterization of femoral component initial stability and cortical strain in a reduced stem-length design. *J Arthroplasty*. 2017;32:601–609.

23. Ali AM, Newman SDS, Hooper PA, Davies CM, Cobb JP. The effect of implant position on bone strain following lateral unicompartmental knee arthroplasty. *Bone Joint Res*. 2017;6:522–529.

24. Small SR, Rogge RD, Malinzak RA, et al. Micromotion at the tibial plateau in primary and revision total knee arthroplasty: fixed versus rotating platform designs. *Bone Joint Res*. 2016;5:122–129.

25. Small SR, Berend ME, Howard LA, Tunç D, Buckley CA, Ritter MA. Acetabular cup stiffness and implant orientation change acetabular loading patterns. *J Arthroplasty*. 2013;28:359–367.

26. Meding JB, Small SR, Jones ME, Berend ME, Ritter MA. Acetabular cup design influences deformational response in total hip arthroplasty. *Clin Orthop Relat Res*. 2013;471:403–409.

27. ASTM International. *ASTM F2028-14, Standard Test Methods for Dynamic Evaluation of Glenoid Loosening or Disassociation*. West Conshohocken: ASTM International; 2014.

28. Anglin C, Tolhurst P, Wyss UP, Pichora DR. Glenoid cancellous bone strength and modulus. *J Biomech*. 1999;32:1091–1097.